Journal of Zhejiang University-SCIENCE A (Applied Physics & Engineering) 2022 23(11):863-881
www.jzus.zju.edu.cn; www.springer.com/journal/11582
E-mail: jzus_a@zju.edu.cn

Research Article

https://doi.org/10.1631/jzus.A2200215

Check for updates

Soil effect on the bearing capacity of a double-lining structure under internal water pressure

Dong-mei ZHANG[1,2]✉, Xiang-hong BU[1], Jian PANG[3], Wen-ding ZHOU[1], Yan JIANG[4,5], Kai JIA[4], Guang-hua YANG[4]

[1]*Department of Geotechnical Engineering, Tongji University, Shanghai 200092, China*
[2]*Key Laboratory of Geotechnical and Underground Engineering of Minister of Education, Tongji University, Shanghai 200092, China*
[3]*State Grid Tianjin Electric Power Company Construction Branch, Tianjin 300143, China*
[4]*Guangdong Research Institute of Water Resources and Hydropower, Guangzhou 510610, China*
[5]*School of Water Conservancy Engineering, Zhengzhou University, Zhengzhou 450001, China*

Abstract: Water conveyance tunnels usually experience high internal water pressures and complex soil conditions. Therefore, shield tunnels with double-lining structure have been adopted because of their high bearing capacity. The effect of the interface between the segmental and inner linings on the bearing capacity has been widely investigated; however, the effect of soil on the internal water pressure bearing capacity has not been emphasized enough. Therefore, in this study, model tests and an analytical solution are presented to elucidate the effect of soil on the internal water pressure bearing capacity. First, model tests are conducted on double-lining models under sandy soil and highly weathered argillaceous siltstone conditions. The internal force and earth pressure under these different soil conditions are then compared to reveal the contribution of soil to the internal water pressure bearing capacity. Following this, an analytical solution, considering the soil–double-lining interaction, is proposed to further investigate the contribution of the soil. The analytical solution is verified with model tests. The analytical solution is in good agreement with the model test results and can be used to evaluate the mechanical behavior of the double-lining and soil contribution. The effect of soil on the bearing capacity is found to be related with the elastic modulus of the soil and the deformation state of the double-lining. Before the double-lining cracks, the sandy soil contributes 3.7% of the internal water pressure but the contribution of the soil rises to 10.4% when it is the highly weathered argillaceous siltstone. After the double-lining cracks, the soil plays an important role in bearing internal water pressure. The soil contributions of sandy soil and highly weathered argillaceous siltstones are 10.5% and 27.8%, respectively. The effect of soil should be considered in tunnel design with the internal water pressure.

Key words: Shield tunnel; Double-lining; Bearing capacity; Soil condition; Internal water pressure

1 Introduction

Water conveyance tunnels have gained wide popularity in engineering applications owing to the scarcity of water resources in metropolitan areas. Due to long-distance water diversion and shortage of underground space in urban areas, water conveyance tunnels are deeply buried and consequently experience high internal water pressure and complex surrounding soil conditions (Huang et al., 2019, 2020; Zhang JZ et al., 2021). Therefore, a shield tunnel with double-lining structure has been proposed. The shield method presents advantages such as fast construction speeds and minimal disturbance to the surrounding soil (Li et al., 2021; Huang et al., 2022a, 2022b). The double-lining structure is composed of segmental and reinforced concrete inner linings and demonstrates a higher bearing capacity compared with a monolayer-lined structure (Takamatsu et al., 1992; Guo CX et al., 2019; Zhai et al., 2020).

The bearing capacity of a shield tunnel with a double-lining structure under internal water pressure has attracted considerable research attention and researchers have suggested that the interface between the

✉ Dong-mei ZHANG, dmzhang@tongji.edu.cn
Xiang-hong BU, https://orcid.org/0000-0002-4677-519X

Received Apr. 18, 2022; Revision accepted Aug. 11, 2022;
Crosschecked Oct. 17, 2022

outer segmental lining and the inner lining is a key factor influencing its bearing capacity (Su and Bloodworth, 2016; Liu et al., 2019). Before the inner lining is cast in-situ, the inner surface of the segmental lining can be treated with by a different construction method, such as chiseling, spreading waterproofing membrane, or embedding steel bars. Consequently, the ability of the lining–lining interface to transform shear and normal forces varies and exerts an influence on the bearing capacity of the double-lining. Some researchers have proposed lining–lining interface models to describe the mechanical property of the lining–lining interface. The lining–lining interface construction method influences the smoothness of the interface. International Tunnelling Association (ITA) (Working Group No. 2, International Tunnelling Association, 2000) suggested that only the normal force can be transmitted through the lining–lining interface when the interface is smooth. When the interface is uneven or dowelled jointing, both normal and shear forces can be transmitted through it. Further, Zhang et al. (2001a, 2001b) and Yan et al. (2015) proposed radial and tangential springs to simulate the ability of the lining interface to transmit normal and shear forces. Based on the lining–lining interface model, the mechanical behavior of the double-lining structure has been investigated (Song et al., 2018; Chen et al., 2020; Zhang XD et al., 2021). Wang et al. (2019a, 2019b) conducted the model tests for double-lining possessing different interface types. The results indicated that when the lining–lining interface can transmit both the normal and shear forces, the maximum displacement of double-lining is smaller and failure occurs later. Yang et al. (2018) simulated the lining–lining interface using springs in their 3D finite element models. The results suggested that, as the compression stiffness of normal springs decreased, less internal water pressure was transmitted to the segmental lining.

The research described above has paid most attention to the effect of the lining–lining interface property on the bearing capacity of double-lining and, so far, the effect of surrounding soil has been conventionally regarded as an external load. The stress distribution of soil under internal water pressure has been studied for that high minimum principal stresses of soil would lead to the hydraulic fracture of soil and to local water losses (Schleiss, 1997; Simanjuntak et al., 2014; Zhou et al., 2015). In fact, the soil also provides resistance to constrain tunnel deformation under internal water pressure, but this effect of soil on bearing internal water pressure has been ignored.

In this study, considering the soil–double-lining interaction, the bearing capacity of the double-lining structure under internal water pressure is investigated through model tests and an analytical solution. First, double-lining model tests under sandy soil and highly weathered argillaceous siltstone conditions are conducted. A double-lining model is specifically designed to simulate its performance under internal water pressure. By comparing the behavior of the double-lining model under different soil conditions, the contribution of soil to the bearing capacity of the double-lining is analyzed. Subsequently, an analytical solution for the soil–double-lining interaction under internal water pressure is proposed and verified against the model test results. The bearing contribution of soil to the internal water pressure is found to be closely related to the elastic modulus of the soil.

2 Design of the model test

2.1 Loading system and loading process

Figs. 1 and 2 present the loading system designed for the model test. The loading system consisted of a model box with external earth pressure and internal water pressure loading devices. The model box was 1.8 m high, 2.0 m wide, and 0.4 m thick internally. Two transparent Perspex plates with square shapes and a dimension of 0.8 m×0.8 m were placed in the middle of the model box to enable convenient observation during the loading process. A circular opening was made in the middle of the transparent Perspex plate to facilitate the entry of water bladder into the tunnel.

Three hydraulic jacks were set above the soil to simulate the external earth pressure acting on the shield tunnel buried 50 m deep. A distribution frame with a high bending stiffness was designed to transform the point load into a distribution load. The internal water pressure loading device included a water bladder, water pressure pump, and automatic pressure controller. The water bladder was composed of an elastic latex membrane, steel cover plates, and steel sealing rings. After the water bladder was filled with water, the internal water pressure was transmitted to the inner surface of the tunnel lining through the latex membrane. The

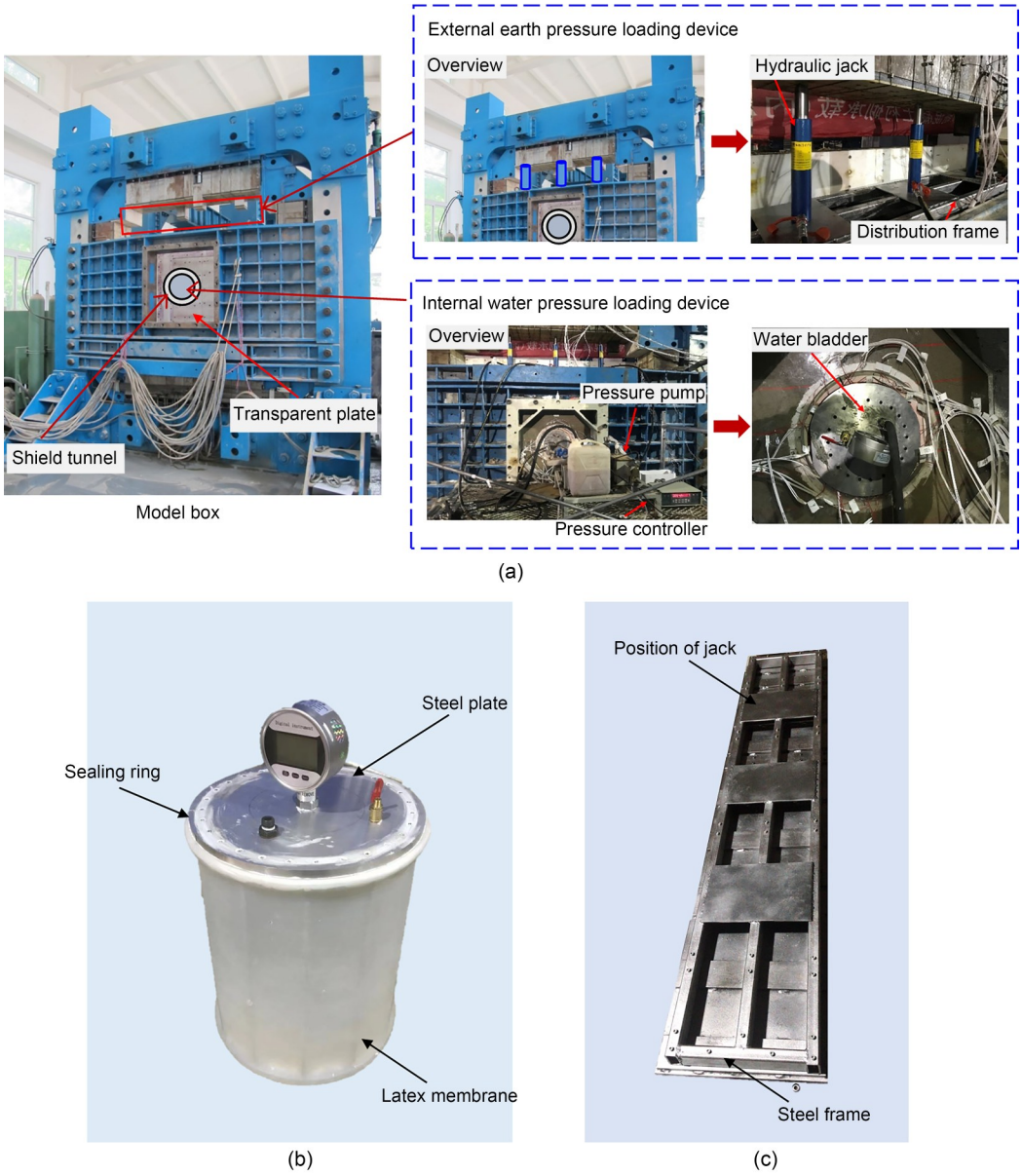

Fig. 1 Loading system designed for the model test under internal water pressure conditions: (a) system composition; (b) water bladder; (c) distribution frame

water bladder was 420 mm in length, longer than that of the tunnel, to ensure that the water pressure was uniform along the tunnel.

The loading process involved two steps. First, external earth pressure was loaded through the hydraulic jacks. The buried depth of tunnel crown was 50 m and the corresponding earth pressure was 900 kPa. In order to study the mechanical behavior of double-lining under different loads, the external earth pressure was loaded to 360, 720, and 900 kPa step by step. Each earth pressure step was kept stable for 30 min until the movement of soil stopped. The internal water pressure was increased by 0.01 MPa until the failure of the double-lining structure. Each water pressure step was kept for 5 min until the soil deformation reached stability.

2.2 Similarity relation

It has been established that a physical quantity is required to follow the similarity relation between a prototype and a model. In this model test, the similarity ratios of geometry C_L and unit weight C_γ were selected

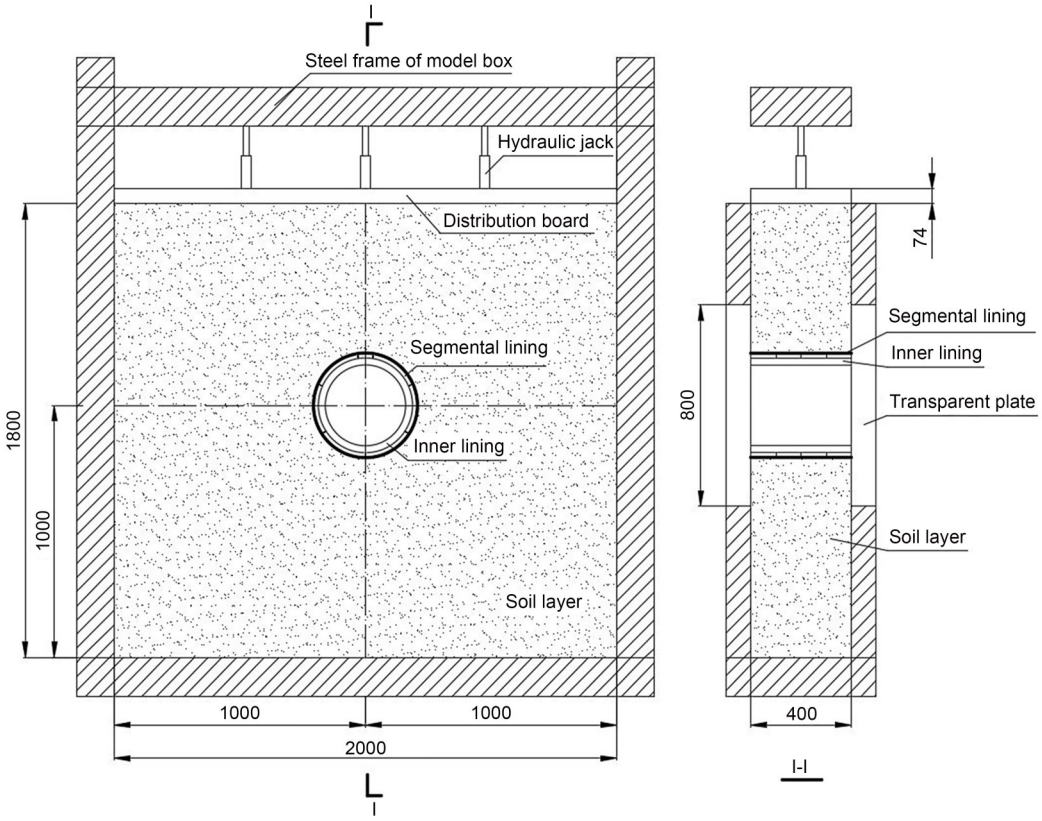

Fig. 2 Schematic of the model box (unit: mm)

as the basic similarity ratios. C_L was determined to be 1:20 by considering the boundary effect of the model box and the size of the tunnel model. In the 1*g* experimental condition (*g* denotes the acceleration of gravity), the similarity ratio of unit weight C_γ was determined to be 1:1. The similarity ratios for other quantities were similarly determined, and the values obtained are presented in Table 1.

Table 1 Similarity ratios in this model test

Physical quantity	Symbol	Similarity relation	Similarity ratio
Geometry	L	C_L	1:20
Unit weight	γ	C_γ	1:1
Elastic modulus	E	$C_E=C_L\times C_\gamma$	1:20
Stress	σ	$C_\sigma=C_L\times C_\gamma$	1:20
Pressure	q	$C_q=C_L\times C_\gamma$	1:20
Strain	ε	C_ε	1:1
Axial stiffness	EA	$C_{EA}=C_L^3\times C_\gamma$	$1:20^3$
Axial stiffness coefficien	k	$C_k=C_L^2\times C_\gamma$	$1:20^2$
Flexural stiffness	EI	$C_{EI}=C_L^5\times C_\gamma$	$1:20^5$
Axial force	N	$C_N=C_L^3\times C_\gamma$	$1:20^3$
Moment	M	$C_M=C_L^4\times C_\gamma$	$1:20^4$

2.3 Modelling of double-lining

Fig. 3 presents a cross-sectional view of the prototype shield tunnel. As can be observed, the double-lining structure is composed of a segmental lining, an

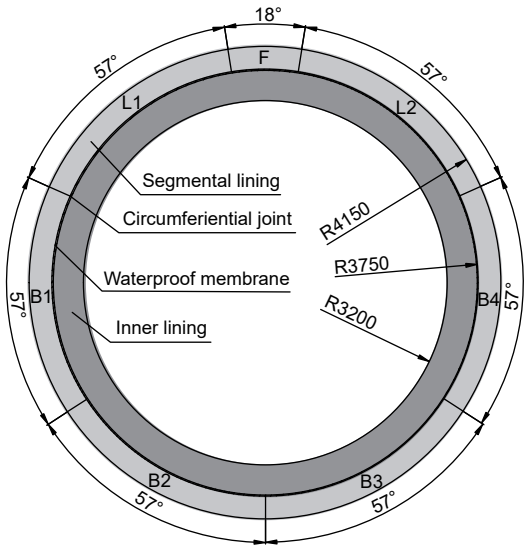

Fig. 3 Prototype of the shield tunnel with a double-lining structure (unit: mm)

inner lining, and a waterproof membrane. The segmental lining consists of one key block (F), two adjacent blocks (L1 and L2), and four standard blocks (B1–B4). The external radius of the segmental lining is 4.15 m, and the inner radius is 3.75 m. The concrete type used is C55, and the width of the segment is 1.60 m. The inner lining is cast in place using C50 grade concrete. The inner diameter of the inner lining is 6.4 m. A 1.2 mm-thick waterproof membrane is spread between the segmental and inner linings to enhance the waterproofing ability of the tunnel.

Fig. 4 presents the 3D and cross-sectional views of the double-lining model. The model test was designed to investigate the behavior of double-lining in the cross-section. The earth pressure, internal water pressure, and the soil were kept identical along the longitudinal direction. For the double-lining structure, the segmental lining was a staggered assembly with a 38° rotational shift to the adjacent rings. Therefore, four rings of tunnel of 0.4-m length are two cycles of the staggered installation of the segmental lining and can represent the double-lining structure. To simulate the mechanical response of the double-lining structure under internal water pressure, the lining material, joint configuration, and lining interface were specifically designed.

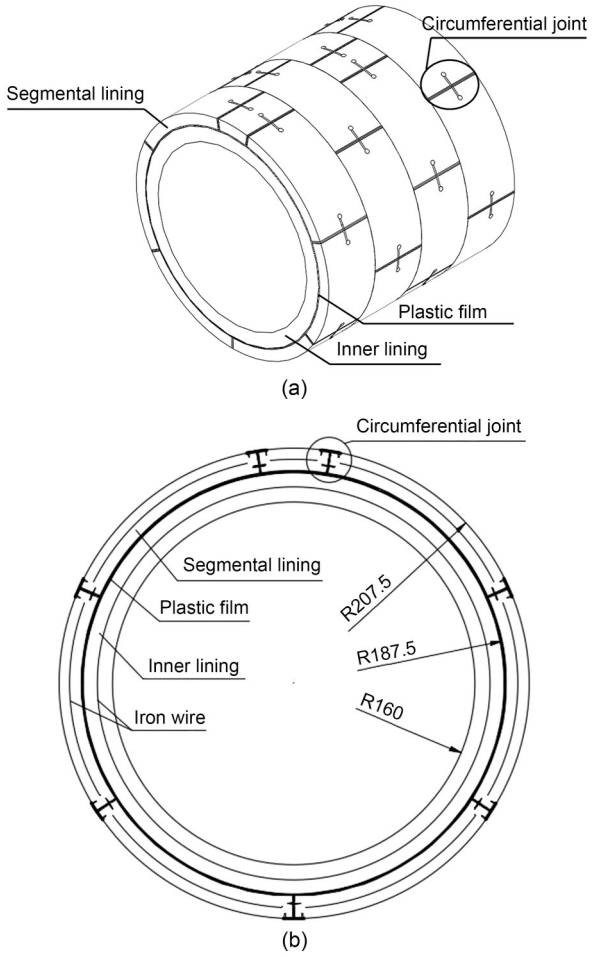

Fig. 4 Schematic of the double-lining model: (a) 3D view; (b) cross-sectional view (unit: mm)

2.3.1 Similar materials for the linings

The concrete of the segmental and inner linings was simulated using gypsum mortar. Gypsum mortar is a mixture of gypsum, water, and diatomite. It is necessary for the concrete and gypsum mortar to satisfy the similarity ratios of elastic modulus and compressive strength. Therefore, uniaxial compressive strength tests were conducted on gypsum mortar specimens containing different gypsum contents. The test results are presented in Fig. 5. Based on the similarity ratio, a gypsum mortar mixed with water, gypsum, and

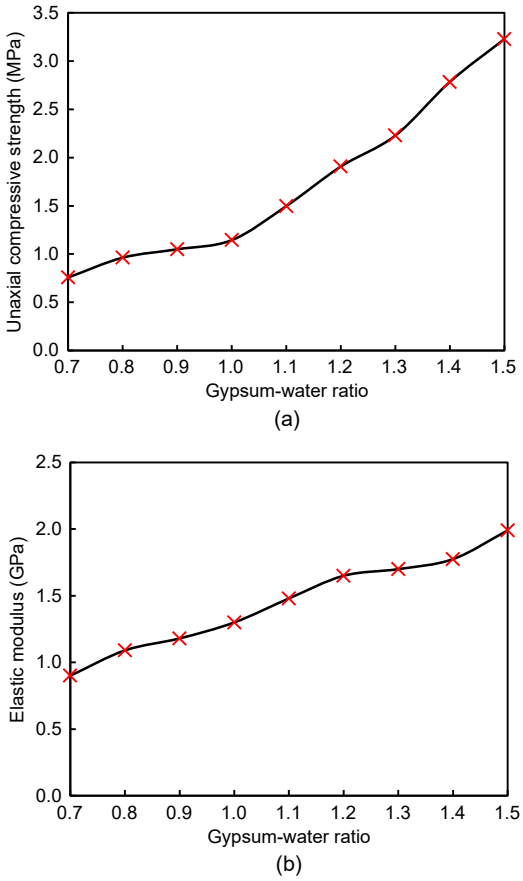

Fig. 5 Test results for the gypsum mortar: (a) uniaxial compressive strength; (b) elastic modulus

diatomite in a ratio of 1.0:1.4:0.1 was adopted for the segmental lining and one with a ratio of 1.00:1.35:0.10 was adopted for the inner lining. The mechanical parameters of the segmental and inner linings are presented in Table 2.

Table 2 Mechanical properties of the double-lining

Item	Segmental lining		Inner lining	
	E (GPa)	$f_{cu,k}$ (MPa)	E (GPa)	$f_{cu,k}$ (MPa)
Prototype	35.5	55	34.5	50
Model	1.71	2.81	1.67	2.54
Actual similarity ratio	1:20.76	1:19.57	1:20.65	1:19.69

E and $f_{cu,k}$ refer to the elastic modulus and uniaxial compressive strength of materials

Iron wire was used to simulate the rebar in the segmental and inner linings. In the presence of internal water pressure, the lining is expected to crack under the action of the tensile force produced in the lining. After the lining cracks, the rebar primarily bears the tension. Therefore, the arrangement of the iron wire was that the similarity ratio of axial stiffness C_{EA} (1:20^3) was obeyed. The elastic modulus of the iron wire and rebar is 200 GPa. The reinforcement ratio of the segment in the prototype is 0.9%. Therefore, two iron wires with diameters of 0.8 mm were arranged in each segmental lining. The reinforcement ratio of the inner lining in the prototype was 2.3%. Accordingly, 16 rings of iron wires with diameters of 1.0 mm were set in the inner lining of the model.

2.3.2 Modelling of the segmental joint

Simulating a segmental circumferential joint is one of the primary challenges faced during the execution of the model test. Wang et al. (2019a, 2019b) and Guo R et al. (2019) proposed the creation of grooves at the joint position in the gypsum mortar ring. This method could effectively simulate the bending stiffness of the joint. However, it is not reasonable to simulate the tension capacity of the joint accurately. Under the effect of internal water pressure, the joint is under tension and bears the existing load through bolts. In this condition, the gypsum mortar ring with grooves cracks and cannot withstand the tension. To overcome this shortcoming, a novel approach for modelling the segmental joints was proposed. As shown in Fig. 6, the joint model was composed of two iron pieces, two

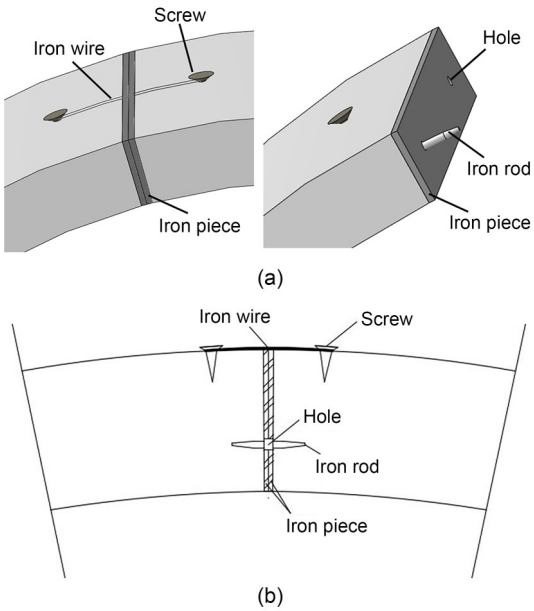

Fig. 6 Detailed illustration of the circumferential joint: (a) 3D view; (b) cross-sectional view

iron rods, two screws, and an iron wire. To simulate the mechanical behaviour of a real joint, the bending stiffness and tension stiffness of the joint should satisfy a similar relation between the model and prototype. The iron rods were set at the hole of the iron plates to simulate the bending stiffness of the joint. The geometric size of the iron rod was determined through a similar relation of bending stiffness, and the bending stiffness of the joint was obtained by numerical simulation. The diameter and length of the iron rod were 1.6 and 25.0 mm, respectively. The iron wire was set to simulate the tension capacity of the joint, fixed at the external surface of segment by a screw. The iron wire of the model and the bolt of the prototype should satisfy a similar relation of tension stiffness coefficient, as shown in Eq. (1).

$$\frac{E_{\mathrm{m}}A_{\mathrm{m}}}{l_{\mathrm{m}}}=C_k\frac{E_{\mathrm{p}}A_{\mathrm{p}}}{l_{\mathrm{p}}}, \tag{1}$$

where E, A, and l refer to the elastic modulus, area, and length, and subscripts m and p refer to the iron wire and bolt, respectively. $A=\pi D^2/4$, and D refers to the diameter. C_k refers to the similarity ratio of the tension stiffness coefficient and is equal to 1:20^2. In this study, $E_{\mathrm{p}}=E_{\mathrm{m}}=200$ GPa, $D_{\mathrm{p}}=36$ mm, and $l_{\mathrm{p}}=435$ mm. Thus, the iron wire was adopted as $D_{\mathrm{m}}=0.6$ mm and $l_{\mathrm{m}}=30$ mm.

2.3.3 Modelling of the lining–lining interface

According to ITA (Working Group No. 2, International Tunnelling Association, 2000), the double-lining structure can be divided into a double-shell structure and the composite structure based on the lining–lining interface smoothness. For the double-shell structure, the interface is relatively smooth, and only the normal force can be transmitted through the interface. For the composite structure, the interface undergoes chiselling, grooving, or embedding rebars. Both the normal and shear forces can be transmitted through the interface. For the shield tunnel subjected to internal water pressure, laying a waterproof membrane between the inner and segmental linings is generally essential. The surface of the waterproof layer then becomes smooth, and the tunnel can be considered as a double-shell structure. Therefore, in the model test, a smooth plastic film was set inside the segmental lining to simulate the interface with a waterproof layer, as shown in Fig. 7.

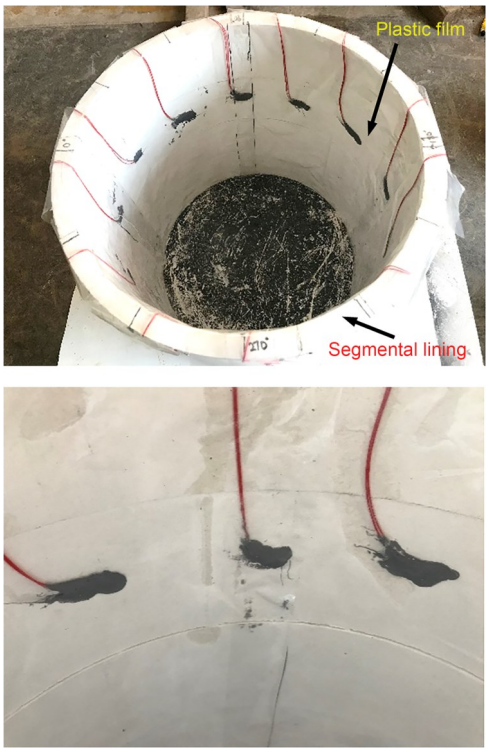

Fig. 7 Modelling of the lining–lining interface

2.4 Modelling of soil

Under the effect of internal water pressure, the shield tunnel deforms outwards, and soil provides the necessary resistance to constrain the resulting tunnel deformation. The tunnel lining and the surrounding soil collectively bear the internal water pressure. The soil resistance is closely related to the elastic modulus of the soil. The elastic modulus must satisfy the similarity ratio. To investigate the influence of the soil condition on the bearing capacity of the double-lining structure, two types of soils were prepared: sandy soil and highly weathered argillaceous siltstone. Sandy soil was simulated using a material composed of barite powder, plastic foam, glass sand, and glycerol. Plastic foam, glass sand, and glycerol were mixed in a volume ratio of 1.0:1.0:0.5. Following this, barite powder was combined with the mixture in a mass ratio of 1:1. The highly weathered argillaceous siltstone condition was simulated using river sand. Through geotechnical tests, the elastic modulus of sandy soil and highly weathered argillaceous siltstone were determined to be 2.5 and 50.0 MPa, respectively, which corresponded to the respective values of 50 MPa and 1 GPa in the prototype.

2.5 Layout of measurement

To evaluate the mechanical behaviour of double-lining tunnels under the effect of internal water pressure, the lining internal force and earth pressure acting around the tunnel were measured, as shown in Fig. 8. For this, strain gauges were arranged at 12 different sections around the circumference and are denoted as S1–S12. The strain gauges were installed on the outer and inner surfaces of the double-lining and lining–lining interface at every section. These strain gauges were used to calculate the internal force acting on the segmental and inner linings. Additionally, earth pressure cells were installed at 45° intervals on the soil–lining interface and are denoted as P1–P8.

3 Test results and analysis

In this section, the internal force and earth pressure under different soil conditions were compared to investigate the effect of soil on the bearing capacity of the double-lining structure. Also, the failure mode of the double-lining structure under high internal water pressure was analysed. The bending moment and axial force can be obtained using Eq. (2).

$$M=\frac{1}{12}\times(\varepsilon_2-\varepsilon_1)\,Ebh^2, \tag{2a}$$

$$N=\frac{(\varepsilon_1+\varepsilon_2)}{2}\times Ebh, \tag{2b}$$

where M and N are the bending moment and axial force, respectively; ε_1 and ε_2 are the strains at the external and inner surfaces of the segmental and inner linings, respectively; b and h are the width and thickness of the segmental and inner linings, respectively.

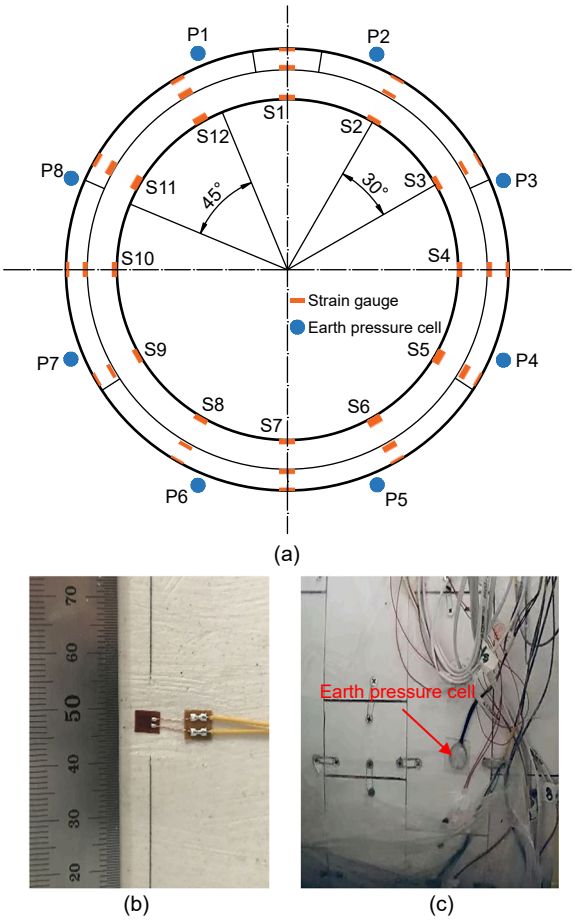

Fig. 8 Layout of measuring point: (a) distribution diagram; (b) strain gauge; (c) earth pressure cell

3.1 Internal force

3.1.1 Bending moment

Fig. 9 illustrates the variation of bending moment with the internal water pressure under the sandy soil and highly weathered argillaceous siltstone conditions. As can be observed, the variation of bending moment due to a change in the internal water pressure was minimal under both the sandy soil and highly weathered

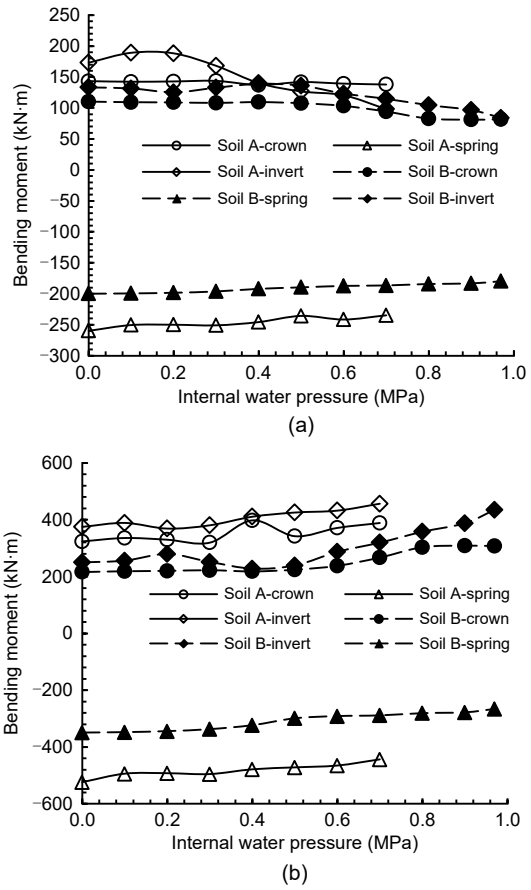

Fig. 9 Bending moment under different soil conditions: (a) segmental lining; (b) inner lining. Soil A: sandy soil; Soil B: highly weathered argillaceous siltstone

argillaceous siltstone conditions. For the segmental lining, the variation of bending moment was mostly less than 50 kN·m, except at the invert under sandy soil conditions. For the inner lining, the largest variation can be observed at the invert under highly weathered argillaceous siltstone conditions, which exceeded 100 kN·m. The variation of bending moment at other positions was within 100 kN·m. Thus, it can be concluded that the bending moment changes slightly during internal water pressure loading regardless of the soil condition.

3.1.2 Axial force

Fig. 10 illustrates the variation of axial force with the internal water pressure under sandy soil and highly weathered argillaceous siltstone conditions. It can be observed that the variation trend followed by the axial force under the sandy soil and highly weathered argillaceous siltstone conditions was similar. When

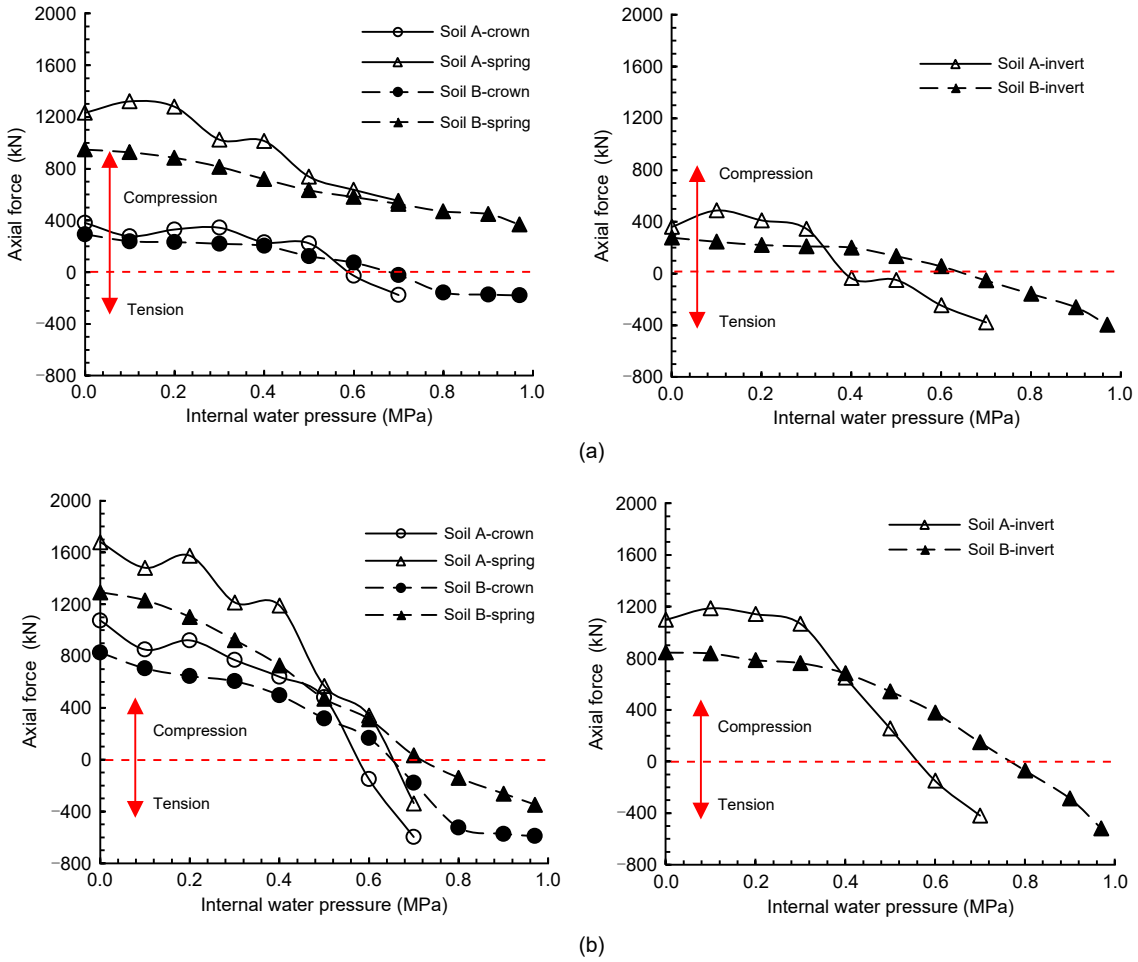

Fig. 10 Axial forces under different soil conditions: (a) segmental lining; (b) inner lining

the earth pressure loading was completed and internal pressure was not applied, the axial force acting on the lining was compressed. With an increase in the internal water pressure, the axial force acting on the segmental and inner linings decreased and developed into tension. The tensile strength of concrete is significantly lower than its compressive strength. Thus, tensile cracks may appear at the double-lining structure. The magnitude of compression at the crown and invert was relatively small compared with that at the spring before the loading of internal water pressure. Therefore, the lining at the crown and invert is more prone to crack formation under the effect of internal water pressure.

However, the variation rate of axial force under the sandy soil condition was found to be larger than that under the highly weathered argillaceous siltstone condition. Considering the segmental lining as an example, the axial force acting at the crown under the sandy soil condition changed from 381.4 to −176.5 kN with an increase in the internal water pressure. The decrement of the axial force was 557.9 kN under the sandy soil condition, which was 18% larger than that observed under the highly weathered argillaceous siltstone condition. As the elastic modulus of soil decreases, the surrounding soil provides less resistance and, consequently, more internal water pressure is borne by the double-lining. In general, under internal water pressure, the axial force acting on the double-lining decreased significantly, whereas the bending moment changed only slightly. The double-lining deforms outwards under the internal water pressure. The radial displacement of double-lining is nearly the same along the circumferential direction. Thus, the double-lining is under tension and no bending deflection occurrs. The axial force changes significantly while the bending

moment changes slightly. The variation rate of the axial force can reflect the sharing ratio of internal water pressure for the double-lining under different soil conditions. The variation rate of axial force for the double-lining structure k_N is defined in Eq. (3), and it was 3218 kN/MPa under the sandy soil condition, and 2111 kN/MPa under the highly weathered argillaceous siltstone condition, which indicated that the sharing ratio of internal water pressure for the double-lining decreased by 35.40%.

$$k_N=\frac{\Delta N}{p_w}, \tag{3}$$

where ΔN is the variation of axial force acting on the double-lining, and p_w is the internal water pressure.

By comparing the variation of axial force between the segmental lining and inner lining, it can be concluded that the axial force decrement for the inner lining is significantly more than that for the segmental lining. Under the highly weathered argillaceous siltstone condition, the axial force decrement for the segmental lining at the crown was 473 kN and that for the inner lining was 1418 kN. The axial force decrement for the inner lining was 3.0, 2.8, and 2.1 times more than that for the segmental lining at the crown, spring, and invert, respectively. The axial force decrement is used to measure the sharing ratio of internal water pressure between the segmental and inner linings, as shown in Eq. (4). The sharing ratio between the segmental and inner linings was 1.0:2.7 and 1.0:2.6 under the sandy soil and highly weathered argillaceous siltstone conditions, respectively. The sharing ratio between the segmental and inner linings is not relevant to the soil condition; however, it is relevant to the lining stiffness. The segmental lining demonstrates low axial stiffness owing to the existence of joints. The inner lining plays an important role in internal water pressure bearing. Thus, the inner lining is more prone to damage under the effect of internal water pressure.

$$\lambda=\frac{\Delta N_s}{\Delta N_i}, \tag{4}$$

where λ refers to the sharing ratio of internal water pressure between the segmental and inner linings, and ΔN_s and ΔN_i refer to the axial force decrement observed for the segmental and inner linings, respectively.

3.2 Earth pressure

3.2.1 Variation in earth pressure under the highly weathered argillaceous siltstone condition

The variation of earth pressure under the highly weathered argillaceous siltstone condition was analysed. Fig. 11 presents the development of earth pressure during external soil loading. It can be observed that the earth pressure increased as the external soil load was imposed. The overburden increased to 20, 40, and 50 m in three steps. The corresponding earth pressure increments at the crown are denoted as Δ1, Δ2, Δ3, respectively. The quantitative relationship can be presented as Δ1≈Δ2≈2Δ3≈340 kPa. After the completion of loading, the earth pressure reached 815 kPa at the crown and 883 kPa at the invert. The earth pressures at the left and right springs were 377 and 469 kPa, respectively. The lateral earth pressure coefficient was 0.45 in the model test.

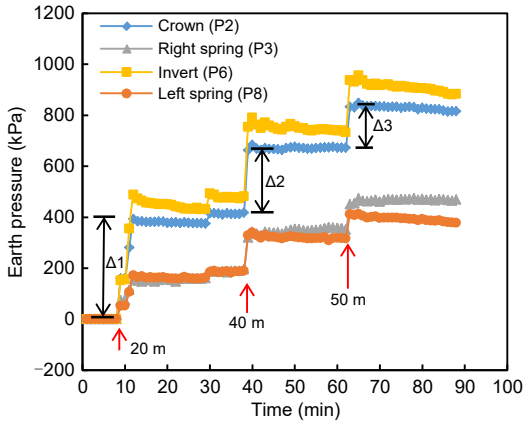

Fig. 11 Variation of earth pressure with external soil load

Fig. 12 presents the variation of earth pressure with the increase of internal water pressure. From the figure, it can be observed that the double-lining structure has undergone the following three stages under the effect of internal water pressure. First, when the internal water pressure was less than 0.4 MPa, the double-lining structure was in the elastic stage. The earth pressure increased almost linearly with the internal water pressure. Second, when the internal water pressure reached 0.4 MPa, the double-lining cracked and subsequently entered the damage stage. The earth pressure still followed a linear trend; however, the rate of increase of earth pressure in the damage state was visibly larger than that observed in the elastic

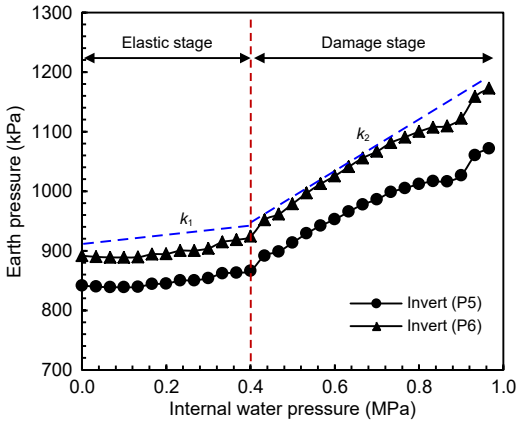

Fig. 12 Variation of earth pressure with internal water pressure

state. Finally, when the internal water pressure increased to 0.97 MPa, the double-lining structure entered a failure stage. At this stage, the joint opening increased sharply and the joint eventually fractured. The segmental lining deformed outward continuously at a constant internal water pressure and, consequently, the double-lining structure lost its bearing capacity.

To compare the soil resistance when the double-lining is in the elastic and damage states, the variation rate of earth pressure with internal water pressure, k_i, is defined as shown in Eq. (5), and the results are presented in Table 3. The variation rate of earth pressure in the damage stage was approximately 3.0 times of that in the elastic stage at the crown and invert, and it was 2.0 times of that in the elastic stage at the left and right springs. When the double-lining cracks, the axial tensile stiffness of the double-lining is reduced. Therefore, the surrounding soil has to bear more internal water pressure. Moreover, the axial forces at the crown and invert are less than those at the spring. Thus, the tensile damages at the crown and invert are more severe. Consequently, the variation rate of earth pressure increases more significantly at the crown and invert.

$$k_i = \frac{\Delta S_i}{\Delta p_{wi}}, \tag{5}$$

where i=1, 2 refers to the elastic and damage stages, respectively; ΔS_i and Δp_{wi} refer to the increments in earth pressure and internal water pressure during the corresponding stage represented by i.

Table 3 Variation rate of earth pressure with internal water pressure

Item		Variation rate	
		k_1 (kPa/MPa)	k_2 (kPa/MPa)
Crown	P1	110	706
	P2	97	456
Right spring	P3	134	408
	P4	88	211
Invert	P5	62	361
	P6	81	438
Left spring	P7	172	325
	P8	94	289

3.2.2 Comparison of earth pressure under different soil conditions

Fig. 13 illustrates the variation in earth pressure under the sandy soil and highly weathered argillaceous siltstone conditions. During the loading process of internal water pressure, the double-lining under the sandy soil condition experienced the following three stages: elastic stage, damage stage, and failure stage. When the internal water pressure reached a cracking point of 0.33 MPa, the double-lining was in the damage stage, and the variation rate of earth pressure increased. When the internal water pressure reached 0.70 MPa, the joint opening increased sharply and the double-lining failed. However, the increment in the earth pressure under the sandy soil condition was obviously less than that under the highly weathered argillaceous siltstone condition. This result indicates that the soil resistance effect demonstrated in the highly weathered argillaceous siltstone condition is significantly higher than that demonstrated in the sandy soil condition, which improves the overall internal pressure bearing capacity of the soil-lining structure.

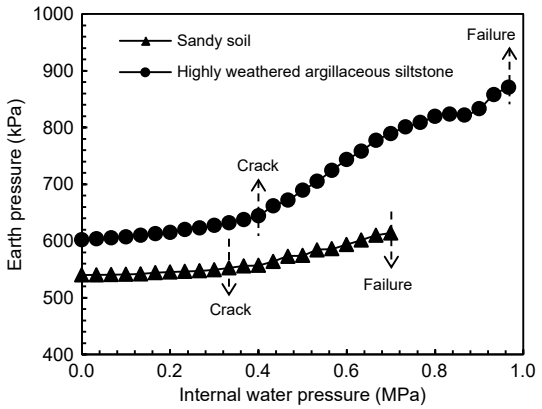

Fig. 13 Earth pressure under different soil conditions

To investigate the contribution of soil and its influence on the bearing capacity of the double-lining, the contribution of soil to the internal water pressure is defined as the ratio of the increment in the earth pressure to the internal water pressure, as shown in Eq. (6). Fig. 14 presents the change in the contribution of soil to the internal water pressure. It can be observed that the contribution of soil to the internal water pressure increased slowly during the elastic stage, whereas it increased rapidly during the damage stage. During the elastic stage, the highly weathered argillaceous siltstone condition contributed 10.4% of the internal water pressure, while the contribution of the sandy soil was only 3.7%. Compared with sandy soil, the contribution of highly weathered argillaceous siltstone was enhanced by only a small margin. Therefore, the cracking point of the double-lining rose slightly from 0.33 to 0.40 MPa. During the damage stage, the contribution to the bearing capacity reached 27.8% for highly weathered argillaceous siltstone and 10.5% for sandy soil. Thus, the contribution of the highly weathered argillaceous siltstone condition was substantially higher than that of the sandy soil condition. Consequently, the ultimate bearing capacity of the double-lining structure increased from 0.70 to 0.97 MPa with a large amplitude when the soil type changed from sandy soil to highly weathered argillaceous siltstone. Thus, the contribution of soil to the internal water pressure increased when the elastic modulus of soil improved, which is beneficial to the joint bearing capacity of the soil-lining.

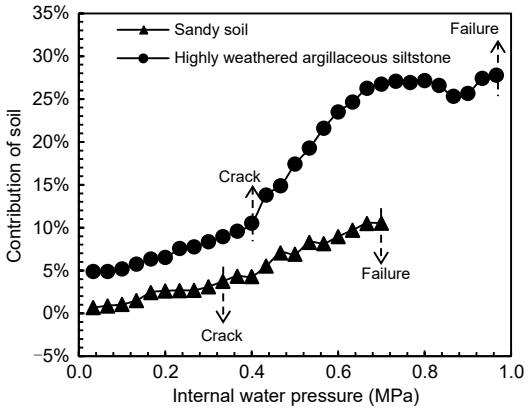

Fig. 14 Contribution of soil under different soil conditions

$$\eta = \frac{\Delta S}{p_{\mathrm{w}}}, \tag{6}$$

where η refers to the contribution of soil to the internal water pressure, and ΔS represents the increment in earth pressure during internal water pressure loading.

3.3 Failure mode

As the internal water pressure increased, tensile cracks continued to appear in the double-lining. The failure characteristics of the double-lining structure were similar under both the sandy soil and highly weathered argillaceous siltstone conditions. The double-lining model after failure under the highly weathered argillaceous siltstone condition is analysed. Fig. 15 shows the crack distribution in the double-lining structure for the final failure state. As can be observed, for the segmental lining, cracks appeared at the crown, spring, and invert. Multiple longitudinal cracks occurred at the crown and invert, whereas the number of cracks at the left and right springs was relatively small. For the inner lining, the crack distribution was similar

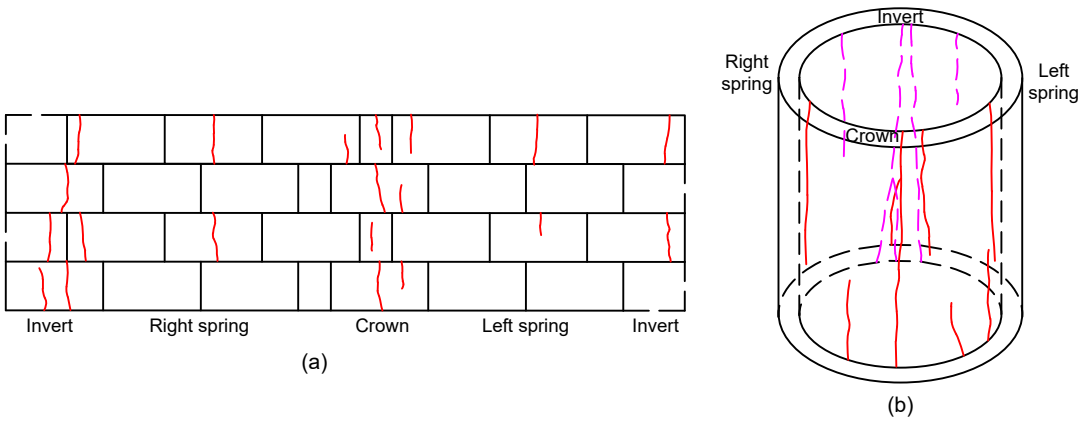

Fig. 15 Crack distribution in the double-lining structure: (a) segmental lining; (b) inner lining

to that of the segmental lining. Cracks were primarily concentrated at the areas of the crown and invert. During the loading of internal water pressure, cracks first appeared at the crown, then at the invert, and finally at the left and right springs. Figs. 16 and 17 present the corresponding images for the segmental and inner linings after failure, respectively. The crack widths at the crown, right spring, invert, and left spring are denoted as D_1, D_2, D_3, and D_4, respectively. For the segmental and inner linings, the crack width relationship can be expressed as $D_1 \approx D_3 > D_4 > D_2$. Thus, it can be concluded that the damage at the crown and invert was more severe. The development of cracks was closely related to the internal force acting on the tunnel, which has been introduced in Section 3.1. The axial force at the crown and invert changed to tension earlier than that at the spring. Consequently, cracks first occurred at the crown and invert. As the internal water pressure increased, the crack number and width at the crown and invert correspondingly increased, and the resulting damage was more severe.

From Figs. 16 and 17, it can be observed that the crack width at the inner lining was larger compared with that at the segmental lining. Additionally, the cracks on the inner lining were mostly longitudinal cracks. This can be attributed to the fact that the inner lining bears a higher proportion of the internal water pressure, which causes severe damage to the inner lining structure.

The double-lining structure failed in the final stage owing to the occurrence of a joint fracture. As can be observed from Fig. 16, the joint fractured and was incapable of withstanding any more tension. Moreover, the cracks in the segmental lining mostly appeared near the joint of the adjacent ring. It can be seen that the cracks in the inner lining usually occurred near a segmental joint. This phenomenon indicates that the segmental joint possesses lower axial stiffness and tensile strength. Thus, the segmental joint can be thought of as a weak-point in the double-lining structure.

In summary, we can conclude that cracks are mostly distributed at the crown and invert near a segmental joint, and more severe damage appears on the inner lining. Thus, the crack width at the crown and invert of the inner lining and close to the segmental joint must be emphasized during the design phase.

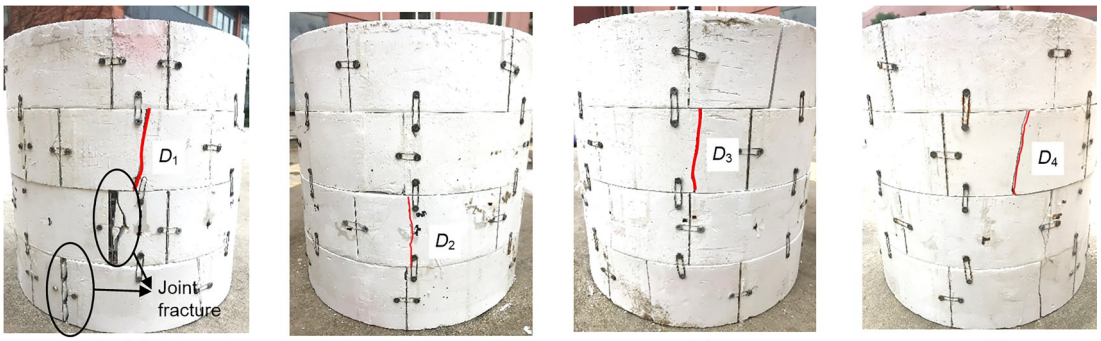

Fig. 16 Object image of the segmental lining after failure: (a) crown; (b) right spring; (c) invert; (d) left spring

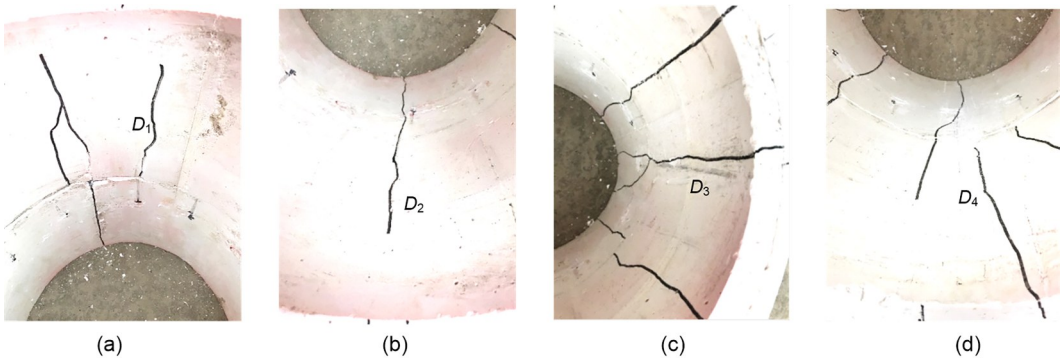

Fig. 17 Object image of the inner lining after failure: (a) crown; (b) right spring; (c) invert; (d) left spring

4 Analytical solution

The model test results indicate that the contribution of soil to the internal water pressure is crucial to the bearing capacity of the double-lining. The contribution of soil is related to the elastic modulus of the soil. To show further the variation of the soil contribution to the internal water pressure with the elastic modulus of the soil, an analytical solution for the double-lining under the effect of internal water pressure is proposed. For this, the segmental and inner linings are assumed to be thick-walled cylinders. The axial stiffness of the segmental lining is affected owing to the existence of joints and the axial stiffness of the inner lining reduces after cracking, which is considered in the analytical solution.

4.1 Analytical model for the interaction between soil and double-lining

4.1.1 Mechanical model

Fig. 18 depicts a mechanical model of the double-lining under the effect of internal water pressure. The double-lining is embedded in an infinite elastic layer of soil. As mentioned earlier, the segmental and inner linings are assumed to be thick-walled cylinders. The elastic modulus and Poisson's ratio of the soil, segmental lining, and inner lining are denoted as E_0, E_1, E_2, v_0, v_1, and v_2, respectively. Moreover, the outer and inner radius of the segmental lining are denoted as r_0 and r_1, respectively, while the inner radius of the inner lining is denoted as r_2.

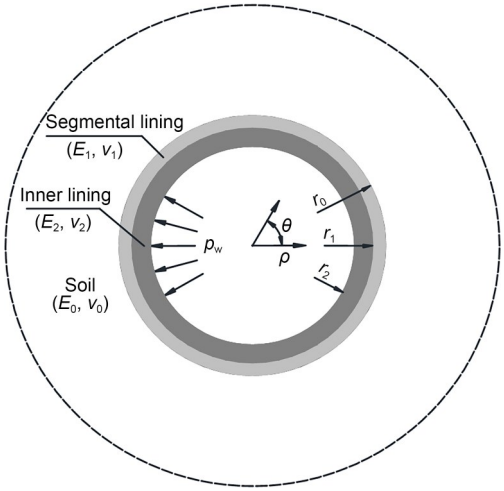

Fig. 18 Mechanical model of the double-lining under internal water pressure. ρ is the radius; θ is the angle

4.1.2 Derivation of the analytical solution

It is known that the internal water pressure p_w is borne by the segmental and inner linings and the soil layer. As shown in Fig. 19, the pressures transmitted to the segmental lining and soil are assumed to be P_1 and P_2, respectively.

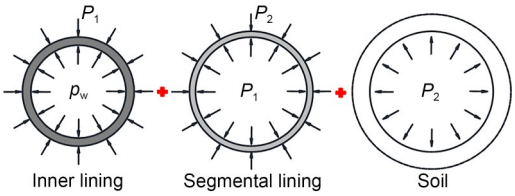

Fig. 19 Load distribution for the tunnel and soil layer

The inner lining, segmental lining, and soil layer can be solved using the Lame solution. According to the Lame solution, the radial displacement function is given as

$$\begin{aligned} u_0 &= \frac{1+v_0}{E_0}\frac{r_0^2}{\rho}P_2, \\ u_1 &= \frac{1+v_1}{E_1(r_0^2-r_1^2)}\left[\frac{r_0^2r_1^2(P_1-P_2)}{\rho}+\right. \\ &\quad \left.(r_1^2P_1-r_0^2P_2)(1-2u_1)\rho\right], \\ u_2 &= \frac{1+v_2}{E_2(r_1^2-r_2^2)}\left[\frac{r_1^2r_2^2(p_w-P_1)}{\rho}+\right. \\ &\quad \left.(r_2^2p_w-r_1^2P_1)(1-2u_2)\rho\right], \end{aligned} \tag{7}$$

where u_0, u_1, and u_2 refer to the radial displacement of the soil layer, segmental lining, and inner lining, respectively.

The radial displacements at the lining–lining interface and soil–lining interface satisfy displacement coordination, as shown in Eq. (8). Further, Eq. (8) can be transformed into a matrix form, and the interface pressure can be solved, as shown in Eq. (9).

$$\begin{cases} u_0\big|_{r=r_0} = u_1\big|_{r=r_0}, \\ u_1\big|_{r=r_1} = u_2\big|_{r=r_1}, \end{cases} \tag{8}$$

$$\begin{bmatrix} (2-2u_1)h_1 & -(h_1+1-2u_1)-\eta_1 \\ 1+(1-2u_1)h_1+\eta_2(h_2+1-2u_2) & -(2-2u_1) \end{bmatrix} \times \begin{bmatrix} P_1 \\ P_2 \end{bmatrix} = \begin{bmatrix} 0 \\ \eta_2(2-2u_2)h_2p_w \end{bmatrix}, \tag{9}$$

where $h_1=\dfrac{r_1^2}{r_0^2}$, $h_2=\dfrac{r_2^2}{r_1^2}$, $\eta_1=\dfrac{E_1(1+u_0)(1-h_1)}{E_0(1+u_1)}$, and $\eta_2=\dfrac{E_1(1+u_2)(1-h_1)}{E_2(1+u_1)(1-h_2)}$.

Then, the stress of segmental and inner linings can be solved according to the Lame solution. The maximum circumferential normal stress occurs at the inner surface of the inner lining, which can be used to determine the cracking load of the double-lining, as shown in Eq. (10).

$$\sigma_{\theta 2}\Big|_{r=r_2}=\frac{\dfrac{r_1^2}{r_2^2}+1}{\dfrac{r_1^2}{r_2^2}-1}p_{\mathrm{w}}-\frac{2}{1-\dfrac{r_2^2}{r_1^2}}P_1, \tag{10}$$

where $\sigma_{\theta 2}$ refers to the circumferential normal stress acting on the inner lining.

4.1.3 Elastic modulus of the segmental and inner linings

As mentioned earlier, the segmental lining is assumed to be a homogeneous thick-walled cylinder. However, the axial stiffness of the circumferential joint is different from that of the segment. Thus, an equivalent elastic modulus was calculated to represent the axial stiffness of the entire segmental lining. As shown in Fig. 20, the segmental lining can be regarded as a tandem system composed of segments and joints under tension. The circumferential displacement of the segmental lining is equal to the sum of the circumferential displacement of the segment and that of the joint, as shown in Eq. (11). Therefore, the equivalent elastic modulus of the segmental lining can be derived as shown in Eq. (12).

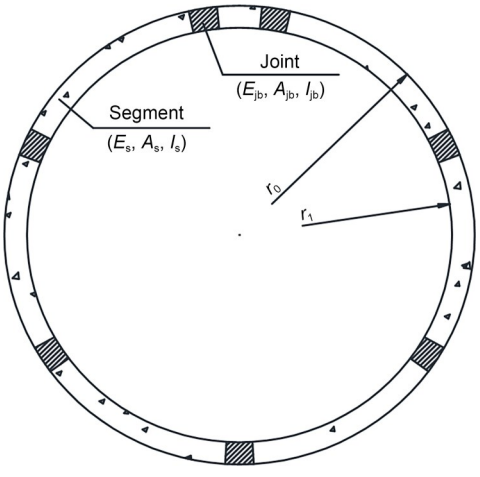

Fig. 20 Schematic of the segmental lining

$$\frac{T_1}{E_1A_s}\left(l_s+l_{jb}\right)=\frac{T_1}{E_sA_s}l_s+\frac{T_1}{E_{jb}A_{jb}}l_{jb}, \tag{11}$$

$$E_1=\frac{l_s+l_{jb}}{\dfrac{l_s}{E_s}+\dfrac{l_{jb}A_s}{E_{jb}A_{jb}}}, \tag{12}$$

where T_1 represents the tensile force acting on the segmental lining; E_s, A_s, and l_s denote the elastic modulus, area, and length of the segment, respectively; E_{jb}, A_{jb}, and l_{jb} represent the elastic modulus, area, and length of the joint bolt, respectively.

After the inner lining cracks, its axial stiffness reduces. The Comité Euro-International du Beton (CEB) model was proposed to describe the mechanical behaviour of reinforced concrete subjected to tension in terms of an average strain (CEB, 1985; Stramandinoli and La Rovere, 2008). The average strain of reinforced concrete with cracks is shown in Eq. (13). Therefore, the axial stiffness of the inner lining after cracking can be derived by Eq. (14).

$$\varepsilon_{2\mathrm{m}}=\varepsilon_{\mathrm{r}}-\Delta\varepsilon_{\mathrm{c}}, \tag{13a}$$

$$\Delta\varepsilon_{\mathrm{c}}=\Delta\varepsilon_{\mathrm{c,\,max}}\frac{T_{2\mathrm{cr}}}{T_2}, \tag{13b}$$

$$\varepsilon_{\mathrm{r}}=\frac{T_2}{E_{\mathrm{r}}A_{\mathrm{r}}}, \tag{13c}$$

$$\Delta\varepsilon_{\mathrm{c,\,max}}=\frac{T_{2\mathrm{cr}}}{E_{\mathrm{r}}A_{\mathrm{r}}}-\frac{T_{2\mathrm{cr}}}{E_{\mathrm{r}}A_{\mathrm{r}}+E_{\mathrm{c}}A_{\mathrm{c}}}, \tag{13d}$$

$$E_2'=\frac{\varepsilon_{2\mathrm{m}}}{\varepsilon_{\mathrm{r}}}\frac{E_{\mathrm{r}}A_{\mathrm{r}}}{A_2}, \tag{14}$$

where $\varepsilon_{2\mathrm{m}}$ represents the average strain on the inner lining; ε_{r} represents the strain in the rebar at a cracked section; $\Delta\varepsilon_{\mathrm{c}}$ represents the contribution of concrete between cracks due to its bond with the rebar; $\Delta\varepsilon_{\mathrm{c,\,max}}$ represents the contribution of concrete at the beginning of the cracking process; T_2 represents the tensile force acting on the inner lining; $T_{2\mathrm{cr}}$ represents the tensile force of the inner lining when cracking; A_2 represents the area of the inner lining; E_{r} and A_{r} denote the elastic modulus and area of the rebar in the inner lining, respectively; E_{c} and A_{c} represent the elastic modulus and area of concrete in the inner lining, respectively; E_2' refers to the elastic modulus of inner lining after cracking.

4.2 Verification of the analytical solution

The analytical solution is verified with the model test conducted under the highly weathered argillaceous siltstone condition. The earth pressures obtained from the model test and analytical solution are compared, as shown in Fig. 21. As can be observed, the earth pressures obtained from the model test and analytical solution are similar, with an average deviation of 7.86%. The cracking point derived by the analytical solution lies at 0.35 MPa, which is close to the cracking point of 0.40 MPa obtained from the model test.

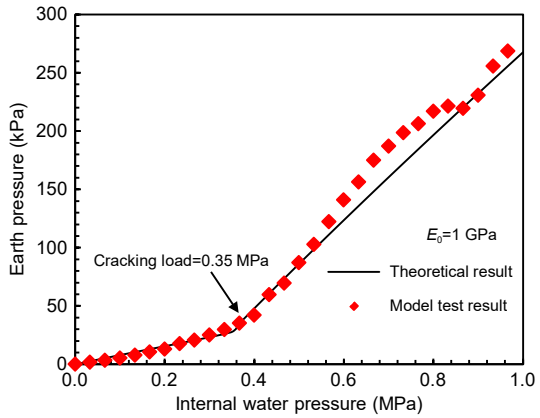

Fig. 21 Comparison between model test and theoretical results

4.3 Effect of soil on the tunnel capacity

The variation in the contribution of soil to the internal water pressure with the internal water pressure is illustrated in Fig. 22. When the double-lining is in the elastic stage, the soil contribution remains stable. After the inner lining cracks, the soil contribution rises and becomes steady with the increase in internal water pressure. For a tunnel lining subjected to internal water pressure, there exist two safety control standards to be followed during the design. First, the cracking point of the lining is selected as a safety control standard. Second, the inner lining is allowed to crack, and the radial displacement of the double-lining is selected as a safety control standard to limit the crack width and joint opening. Therefore, both soil contributions, under the elastic and damage stages, are useful in the design of double-linings.

The variation in the soil contribution to the internal water pressure with the elastic modulus of soil is presented in Fig. 23. As the elastic modulus of the soil increases, the soil contribution rises; however, the rate of increase declines. When the elastic modulus of soil is 50 MPa, the soil contribution under the elastic stage is only 1%, and the soil has little effect on the bearing capacity of the double-lining. The soil contribution under the elastic stage reaches 19.2% when the elastic modulus of soil is 3 GPa. When the double-lining is designed based on the strength control standard, it is suggested that the soil contribution should be considered as the elastic modulus of soil with a value greater than 3 GPa. When the elastic modulus of soil is below 3 GPa, the soil contribution can be used as a reserve of structural safety. Soil contributes to 2.5% of the internal water pressure during the damage stage when the elastic modulus is 50 MPa. When the elastic modulus increases to 500 MPa, the soil contribution reaches 19.1%. When the double-lining is designed using the deformation control standard, the soil contribution must be calculated as the elastic modulus of soil with a value greater than 500 MPa.

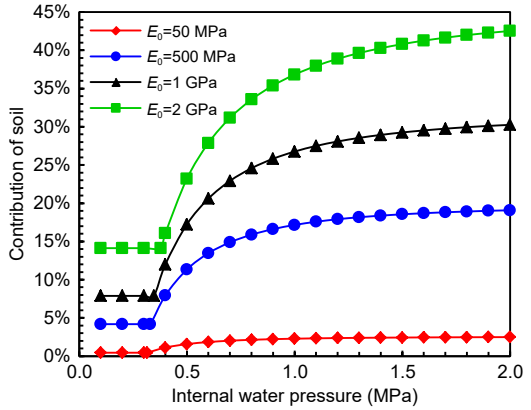

Fig. 22 Variation of soil contribution with internal water pressure

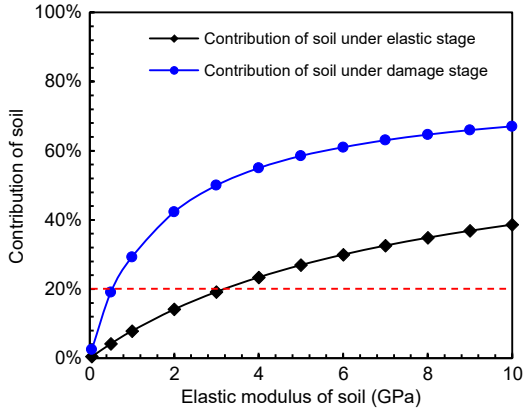

Fig. 23 Variation of soil contribution with the elastic modulus of soil

4.4 Discussion of soil contribution

The results of model tests and analytical solution showed that the contribution of soil on the tunnel bearing capacity increases with an increase of the soil elastic modulus. Consequently, the internal water pressure controlled by double-lining decreases, and the double-lining design can be optimized. Since the inner lining plays a vital role on bearing internal water pressure, the thickness of the inner lining is selected as the optimized design parameter. Under the designed internal water pressure, the thickness of inner lining can be optimized based on the strength or deformation safety control standard.

Fig. 24a shows the thickness of inner lining given the variation of the soil contribution based on the strength safety control standard. It can be observed that the thickness of the inner lining decreases linearly as the soil contribution increases. Taking the internal water pressures of 0.3, 0.4, and 0.5 MPa as the example, when the soil contribution increases from 0 to 50%, the thickness of the inner lining decreases from 0.53 to 0.22 m, from 0.69 to 0.29 m, and from 0.86 to 0.36 m, respectively. The thickness of the inner lining is decreased by about 59%. Furthermore, the reduction in the thickness of the inner lining is independent of the internal water pressure. The soil contribution can decrease the thickness of the inner lining very significantly. In addition, when the soil contribution increases to approximately 90%, the thickness of the inner lining can be reduced to zero, which means the segmental lining is enough to bear internal water pressure and there is no need for an inner lining. Fig. 24b shows the variation of thickness of the inner lining with soil contribution based on the deformation control standard. In this case, the inner lining is allowed to crack, and a joint opening of 2 mm is selected as the deformation control standard. The thickness of the inner lining decreases linearly with soil contribution as well. When the soil contribution increases to 80%, the inner lining is no longer necessary.

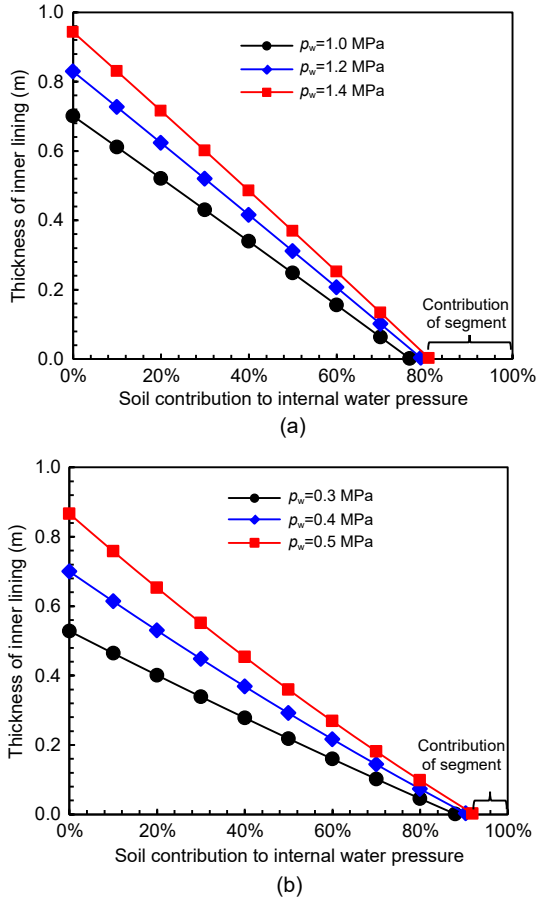

Fig. 24 Thickness of inner lining given the variation of soil contribution: (a) strength control standard; (b) deformation control standard

5 Conclusions

In this study, model tests are conducted to investigate the mechanical responses of double-lining structures under the conditions of sandy soil and of highly weathered argillaceous siltstone. The soil contribution and its influence on the bearing capacity of the double-lining structure are analyzed. An analytical solution for the double-lining structure is proposed to further investigate the variation in the soil contribution to the internal water pressure with the elastic modulus of the soil. The following conclusions can be drawn from the results of the model test and the analytical solution.

(1) The double-lining model is designed in terms of similar material, circumferential joint, and lining–lining interface. The double-lining model is similar to the prototype in its tension stiffness and can simulate the mechanical behaviour of double-lining during the elastic and damage stages.

(2) The proposed analytical solution takes into account the axial stiffness of the segmental lining influenced by the circumferential joint and the reduced axial stiffness of the inner lining after cracking. The average error between the model test and the analytical

solution is approximately 7.9%, which verifies the accuracy of the proposed analytical solution. The analytical solution can reflect the interaction between soil–double-lining and the contribution of soil.

(3) Before the double-lining cracks, the contribution to the bearing capacity of the tunnel is 3.7% for the sandy soil; it increases to 10.4% for the highly weathered argillaceous siltstone. As a result, the double-lining cracks when the internal water pressure is 0.33 MPa under sandy soil, while it cracks at 0.40 MPa under highly weathered argillaceous siltstone.

(4) After the double-lining cracks, the soil plays a more vital role in bearing internal water pressure. The contribution increases to 10.5% for the sandy soil, and 27.8% for the highly weathered argillaceous siltstone. Thus, the ultimate bearing capacity of double-lining rises from 0.70 to 0.97 MPa when the soil condition changes from sandy soil to highly weathered argillaceous siltstone.

(5) The contribution of soil to the bearing capacity increases with the elastic modulus of soil. As the elastic modulus of soil increases to 3 GPa in the elastic stage and 500 MPa in the damage stage, the contribution of soil reaches about 20%, which should be considered at the design stage.

Acknowledgments

This work is supported by the Innovation Program of Shanghai Municipal Education Commission (No. 2019-01-07-00-07-456 E00051), the National Natural Science Foundation of China (Nos. 51978517, 52090082, and 52108381), and the Shanghai Science and Technology Committee Program (Nos. 21DZ1200601 and 20DZ1201404).

Author contributions

Dong-mei ZHANG designed the research. Xiang-hong BU, Jian PANG, and Wen-ding ZHOU conducted the model test for double-lining and processed the corresponding data. Jian PANG and Xiang-hong BU wrote the first draft of the manuscript. Yan JIANG, Kai JIA, and Guang-hua YANG helped to organize the manuscript. Dong-mei ZHANG and Xiang-hong BU revised and edited the final version.

Conflict of interest

Dong-mei ZHANG, Xiang-hong BU, Jian PANG, Wen-ding ZHOU, Yan JIANG, Kai JIA, and Guang-hua YANG declare that they have no conflict of interest.

References

CEB (Comité Euro-International du Beton), 1985. CEB Design Manual on Cracking and Deformation. Bulletin d'information No. 158, Paris, France.

Chen QJ, Wang JC, Huang WM, et al., 2020. Analytical solution for a jointed shield tunnel lining reinforced by secondary linings. *International Journal of Mechanical Sciences*, 185:105813. https://doi.org/10.1016/j.ijmecsci.2020.105813

Guo CX, Han KH, Shi LL, et al., 2019. Superiority analysis of composite structure of initial lining segment and secondary lining molded concrete. *Journal of Coastal Research*, 83(S1):300-304. https://doi.org/10.2112/SI83-049.1

Guo R, Zhang MY, Xie HM, et al., 2019. Model test study of the mechanical characteristics of the lining structure for an urban deep drainage shield tunnel. *Tunnelling and Underground Space Technology*, 91:103014. https://doi.org/10.1016/j.tust.2019.103014

Huang X, Liu W, Zhang ZX, et al., 2019. Exploring the three-dimensional response of a water storage and sewage tunnel based on full-scale loading tests. *Tunnelling and Underground Space Technology*, 88:156-168. https://doi.org/10.1016/j.tust.2019.03.003

Huang X, Liu W, Zhang ZX, et al., 2020. Structural behavior of segmental tunnel linings for a large stormwater storage tunnel: insight from full-scale loading tests. *Tunnelling and Underground Space Technology*, 99:103376. https://doi.org/10.1016/j.tust.2020.103376

Huang ZK, Zhang DM, Pitilakis K, et al., 2022a. Resilience assessment of tunnels: framework and application for tunnels in alluvial deposits exposed to seismic hazard. *Soil Dynamics and Earthquake Engineering*, 162:107456. https://doi.org/10.1016/j.soildyn.2022.107456

Huang ZK, Argyroudis S, Zhang DM, et al., 2022b. Time-dependent fragility functions for circular tunnels in soft soils. *ASCE-ASME Journal of Risk and Uncertainty in Engineering Systems, Part A: Civil Engineering*, 8(3): 04022030. https://doi.org/10.1061/AJRUA6.0001251

Li SH, Zhang MJ, Li PF, 2021. Analytical solutions to ground settlement induced by ground loss and construction loadings during curved shield tunneling. *Journal of Zhejiang University-SCIENCE A (Applied Physics & Engineering)*, 22(4):296-313. https://doi.org/10.1631/jzus.A2000120

Liu DJ, Wang F, Zhang DM, et al., 2019. Interfacial stresses of shield tunnel strengthened by a thin plate at inner surface. *Tunnelling and Underground Space Technology*, 91: 103021. https://doi.org/10.1016/j.tust.2019.103021

Schleiss AJ, 1997. Design of reinforced concrete lining for pressure tunnels and shafts. *International Journal on Hydropower and Dams*, 4(3):88-94.

Simanjuntak TDYF, Marence M, Mynett AE, et al., 2014. Pressure tunnels in non-uniform in situ stress conditions. *Tunnelling and Underground Space Technology*, 42:227-236. https://doi.org/10.1016/j.tust.2014.03.006

Song F, Wang HN, Jiang MJ, 2018. Analytical solutions for lined circular tunnels in viscoelastic rock considering various interface conditions. *Applied Mathematical Modelling*,

55:109-130.
https://doi.org/10.1016/j.apm.2017.10.031

Stramandinoli RSB, La Rovere HL, 2008. An efficient tension-stiffening model for nonlinear analysis of reinforced concrete members. *Engineering Structures*, 30(7):2069-2080.
https://doi.org/10.1016/j.engstruct.2007.12.022

Su J, Bloodworth A, 2016. Interface parameters of composite sprayed concrete linings in soft ground with spray-applied waterproofing. *Tunnelling and Underground Space Technology*, 59:170-182.
https://doi.org/10.1016/j.tust.2016.07.006

Takamatsu N, Murakami H, Koizumi A, 1992. A study on the bending behaviour in the longitudinal direction of shield tunnels with secondary linings. Proceedings of the International Congress Towards New Worlds in Tunnelling, p.277-285.

Wang SM, Jian YQ, Lu XX, et al., 2019a. Study on load distribution characteristics of secondary lining of shield under different construction time. *Tunnelling and Underground Space Technology*, 89:25-37.
https://doi.org/10.1016/j.tust.2019.03.010

Wang SM, Ruan L, Shen XZ, et al., 2019b. Investigation of the mechanical properties of double lining structure of shield tunnel with different joint surface. *Tunnelling and Underground Space Technology*, 90:404-419.
https://doi.org/10.1016/j.tust.2019.04.011

Working Group No. 2, International Tunnelling Association, 2000. Guidelines for the design of shield tunnel lining. *Tunnelling and Underground Space Technology*, 15(3):303-331.
https://doi.org/10.1016/S0886-7798(00)00058-4

Yan QX, Yao CF, Yang WB, et al., 2015. An improved numerical model of shield tunnel with double lining and its applications. *Advance in Materials Science and Engineering*, 2015:430879.
https://doi.org/10.1155/2015/430879

Yang F, Cao SR, Qin G, 2018. Mechanical behavior of two kinds of prestressed composite linings: a case study of the Yellow River crossing tunnel in China. *Tunnelling and Underground Space Technology*, 79:96-109.
https://doi.org/10.1016/j.tust.2018.04.036

Zhai WZ, Chapman D, Zhang DM, et al., 2020. Experimental study on the effectiveness of strengthening over-deformed segmental tunnel lining by steel plates. *Tunnelling and Underground Space Technology*, 104:103530.
https://doi.org/10.1016/j.tust.2020.103530

Zhang HM, Guo C, Lv GL, 2001a. Mechanical model for shield pressure tunnel with secondary linings. *Journal of Hydraulic Engineering*, 32(4):28-33 (in Chinese).

Zhang HM, Che FX, Xia MY, 2001b. Study on loads test of shied tunnel segment reinforced by double linings. *Journal of Tongji University*, 29(7):779-783 (in Chinese).

Zhang JZ, Huang HW, Zhang DM, et al., 2021. Effect of ground surface surcharge on deformational performance of tunnel in spatially variable soil. *Computers and Geotechnics*, 136:104229.
https://doi.org/10.1016/j.compgeo.2021.104229

Zhang XD, Wang JC, Chen QJ, et al., 2021. Analytical method for segmental tunnel linings reinforced by secondary lining considering interfacial slippage and detachment. *International Journal of Geomechanics*, 21(6):04021084.
https://doi.org/10.1061/(ASCE)GM.1943-5622.0002025

Zhou YF, Su K, Wu HG, 2015. Hydro-mechanical interaction analysis of high pressure hydraulic tunnel. *Tunnelling and Underground Space Technology*, 47:28-34.
https://doi.org/10.1016/j.tust.2014.12.004